



# Synthesis of La modified ceria–zirconia solid solution by advanced supercritical ethanol drying technology and its application in Pd-only three-way catalyst

Qiuyan Wang<sup>a</sup>, Guangfeng Li<sup>a</sup>, Bo Zhao<sup>a,b</sup>, Renxian Zhou<sup>a,\*</sup>

<sup>a</sup> Institute of Catalysis, Zhejiang University, Hangzhou 310028, PR China

<sup>b</sup> School of Pharmaceutical and Chemical Engineering, Taizhou University, Taizhou 317000, PR China

## ARTICLE INFO

### Article history:

Received 22 June 2010

Received in revised form 1 September 2010

Accepted 3 September 2010

Available online 21 September 2010

### Keywords:

Ceria–zirconia

Lanthana

Solid solution

Supercritical drying

Pd-only three-way catalysts

## ABSTRACT

In this work, supercritical drying technology is investigated as a new method contrast with the conventional drying techniques to obtain La modified ceria–zirconia solid solution (CZL) with advanced textural/structural properties, and its supported Pd-only three-way catalysts (TWCs) were also prepared and studied. The results demonstrate that the CZL sample prepared by supercritical drying method shows relatively larger specific surface area, better thermal stability and higher redox properties, as well as the prominent oxygen storage capacity compared with samples prepared by conventional drying method. Moreover, it also exhibits remarkable porosity and wide pore size distribution due to the elimination of vapor–liquid interface in the process of supercritical drying, which is beneficial to the adsorption/desorption of pollutant in TWCs. The excellent structural/textural properties of the fore-named CZL support lead to the outstanding catalytic activity, wide air-to-fuel operation window of the corresponding three-way catalyst, indicating its tremendous potential possibilities.

Crown Copyright © 2010 Published by Elsevier B.V. All rights reserved.

## 1. Introduction

Ceria–zirconia solid solution has drawn great attention as an outstanding oxygen storage material in three-way catalysts (TWCs), which can reduce emissions of CO, HC (hydrocarbons) and NO<sub>x</sub> simultaneously [1–6]. The major contributing factor is that ceria–zirconia solid solution shows a large concentration of surface and bulk oxygen-vacant sites, the fast exchange of surface oxygen with gas-phase oxygen species and the high diffusion rates of bulk oxygen toward its surface, which are caused by the presence of a rapid Ce<sup>4+</sup>/Ce<sup>3+</sup> redox couple [7–9].

Up to now, great deals of efforts have been paid to investigate the structure and properties of ceria–zirconia solid solution [10–14], and it was found that the catalytic performance of TWCs correlates to the specific surface area, thermal stability and oxygen exchange capacity (OSC) of samples. Strict restrictions on automotive emissions require higher catalytic activity at lower temperature, and the TWCs are located in positions closer to the engine manifold resultantly. However, the temperature in catalytic converter can rise to even above 1000 °C [15,16], at which the catalyst readily sinters, leading to the loss of specific surface area, oxygen storage capacity and further the decline of catalytic activity [17–19]. Several strategies such as the introduction of rare earth [9,20–23], base metals [13,24–26] and transition metals [27–31] have been recommended in order to improve the properties mentioned above.

On the other hand, the preparation procedure strongly affects the properties of the ceria–zirconia solid solution and the catalytic performance of its supported TWCs. Numerous synthesis routes including ball milling, co-precipitation, sol–gel, combustion, hydrothermal process and so on have been developed to prepare ceria–zirconia or ceria–zirconia-based materials [32–42]. However, both the lower specific surface area and inferior thermal stability are the main encumbrances faced by researchers, accounting for the adoption of common drying method. It is well known that when the removal of the solvent from sample is carried out conventionally in air or in vacuum, the highly porous texture may collapse due to the capillary force at a vapor–liquid interface.

In this paper, supercritical drying was applied as a new method contrast with the conventional drying techniques for the development of La modified ceria–zirconia solid solution (CZL) with higher specific surface area, larger OSC and better thermal stability. An important point, specifically addressed herein, is the investigation of the effects of drying method on the structural/textural properties of CZL and the effects on its supported Pd-only TWCs.

## 2. Experimental procedures

### 2.1. Sample preparation

The La modified ceria–zirconia solid solution samples were prepared as follows. The ammonia solution was slowly added to the quantitative mixed aqueous solution of Ce(NO<sub>3</sub>)<sub>3</sub>·6H<sub>2</sub>O, ZrO(NO<sub>3</sub>)<sub>2</sub>·6H<sub>2</sub>O and La(NO<sub>3</sub>)<sub>3</sub>·6H<sub>2</sub>O under continuous stirring until pH value reached 9.0. The obtained slurry was aged at room

\* Corresponding author. Tel.: +86 571 88273290; fax: +86 571 88273283.

E-mail address: [zhourenxian@zju.edu.cn](mailto:zhourenxian@zju.edu.cn) (R. Zhou).

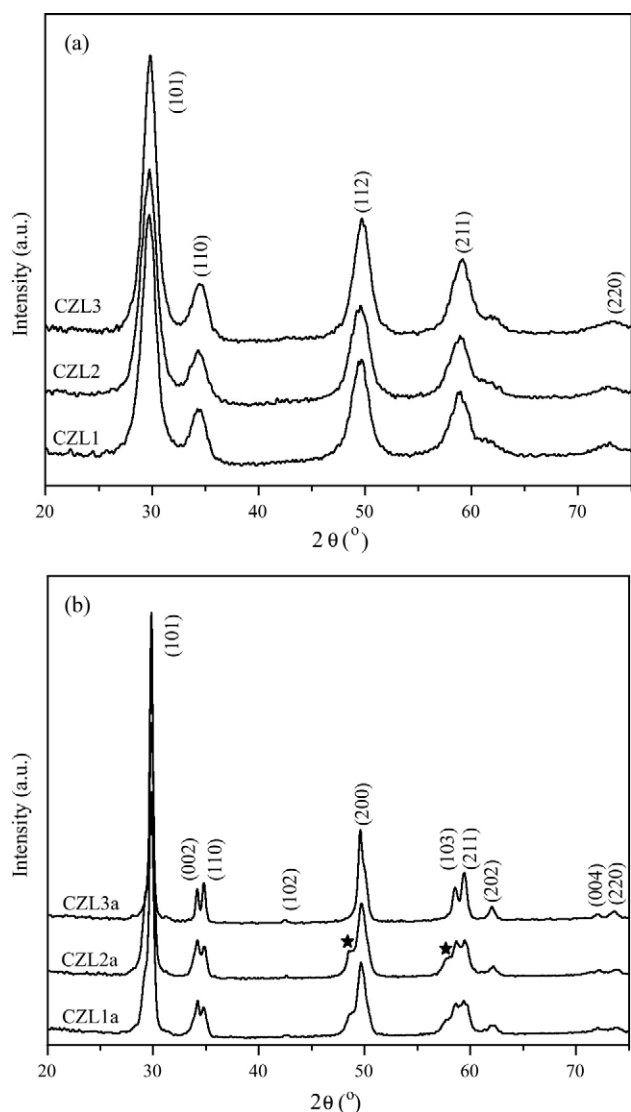


Fig. 1. XRD patterns of fresh (a) and aged (b) supports: (★) deteriorated Ce–Zr–La mixed oxide.

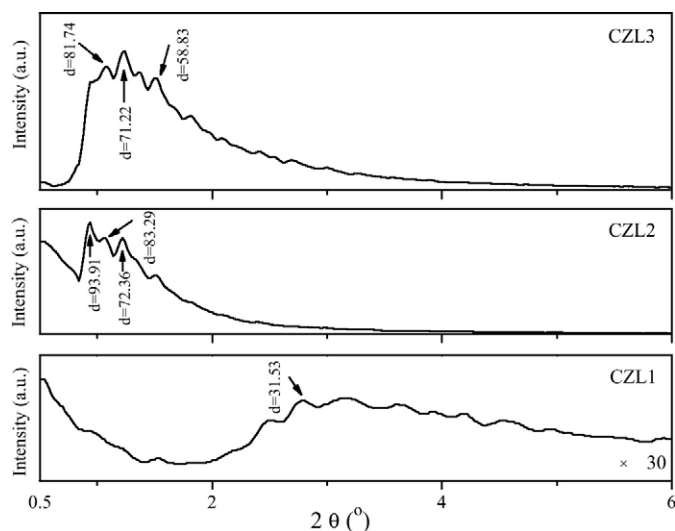


Fig. 2. Small-angle XRD patterns of all the fresh CZLx samples.

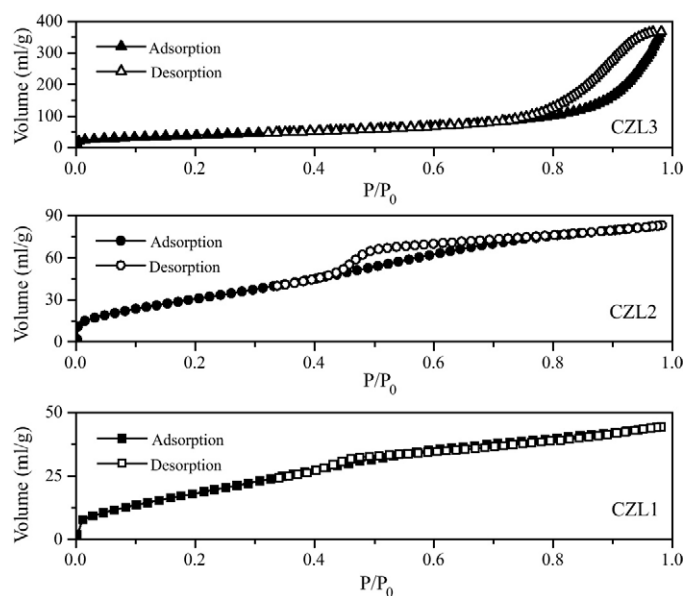


Fig. 3. Nitrogen adsorption/desorption isotherms of the fresh samples.

temperature (20 °C) for 12 h, and then was filtered with a large quantity of distilled water until pH value reached ca. 7. One-third of the resulting precipitate was separated, which was denoted as P1. The remainder precipitate was washed with ethanol furthermore to replace the water in the precipitate, and was divided into two parts, labeled as P2 and P3, respectively. P1 and P2 were dried at 100 °C for 12 h while P3 was dried under supercritical condition in ethanol (265 °C, 7.0 MPa). All of the dried samples were calcined at 500 °C for 4 h in static air (hereafter referred to as CZL1, CZL2 and CZL3, respectively), and then the materials were crushed and sieved to a size range of 40–60 mesh. A portion of the powders were further aged at 1100 °C in static air for 4 h to investigate the thermal stability of the samples, and the aged samples were denoted as CZL1a, CZL2a and CZL3a, correspondingly. The theoretical molar ratio of Ce:Zr is 1:4 and the theoretical additive content of  $\text{La}_2\text{O}_3$  is 5 wt.% for CZL. All the La modified ceria–zirconia solid solution in this study was denoted as CZLx (x means the serial number of the sample) in brief,  $x = 1, 2$ , and 3.

The corresponding Pd/CZLx was prepared by conventional impregnation method with an aqueous of  $\text{H}_2\text{PdCl}_4$  as metal precursor. The impregnated samples were reduced with hydrazine hydrate to de-associate  $\text{Pd}^{2+}$  and  $\text{Cl}^-$  via the transform of  $\text{Pd}^{2+}$  to Pd. Then the reduced sample was filtered and washed with a large amount of deionized water until no  $\text{Cl}^-$  ion was detected in the filtered solution (by  $\text{AgNO}_3$  aqueous), considering that the appearance of Cl is harmful to the catalytic activity. The washed samples were dried at 110 °C for 4 h and then calcined at 500 °C for 2 h in static air due to the active phase in TWC is metal oxide. In order to compare their thermal stability, the catalysts were also calcined at 1100 °C for 4 h (in static air). The academic loading content of Pd for all the catalysts is 0.5 wt.%. The catalysts obtained at 1100 °C are labeled as Pd/CZL1a, Pd/CZL2a and Pd/CZL3a, respectively.

## 2.2. Catalytic activity test

The evaluation of three-way catalytic activity was performed in a fixed-bed continuous flow quartz reactor. The catalyst (0.2 ml) was held in the quartz tube by packing quartz wool at both ends of the catalysts bed, and the back mixing in reactor is minimized by decreasing the dead volume of the reactor. The feed stream was regulated using special mass flow controllers and contained NO

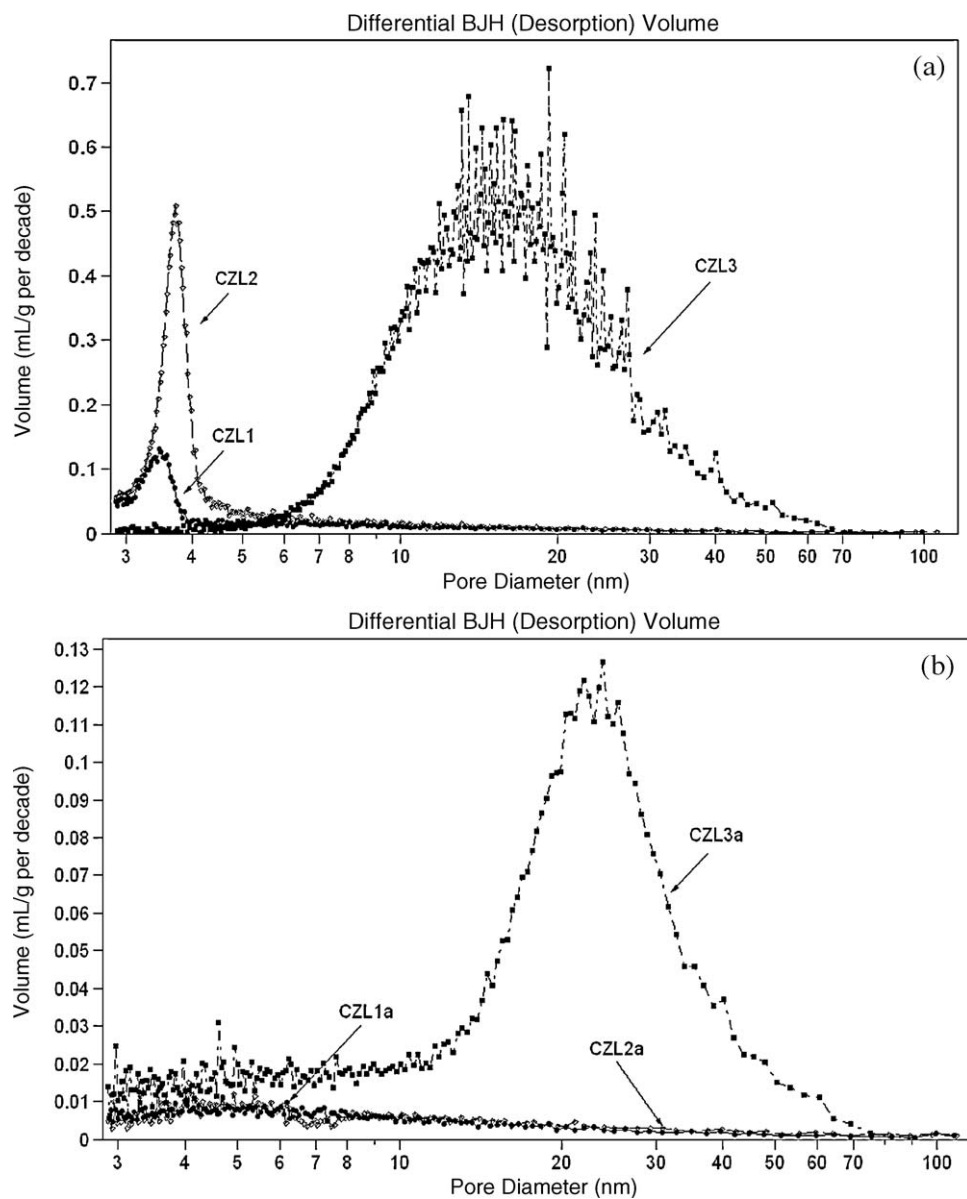


Fig. 4. Pore size distribution of fresh (a) and aged (b) supports.

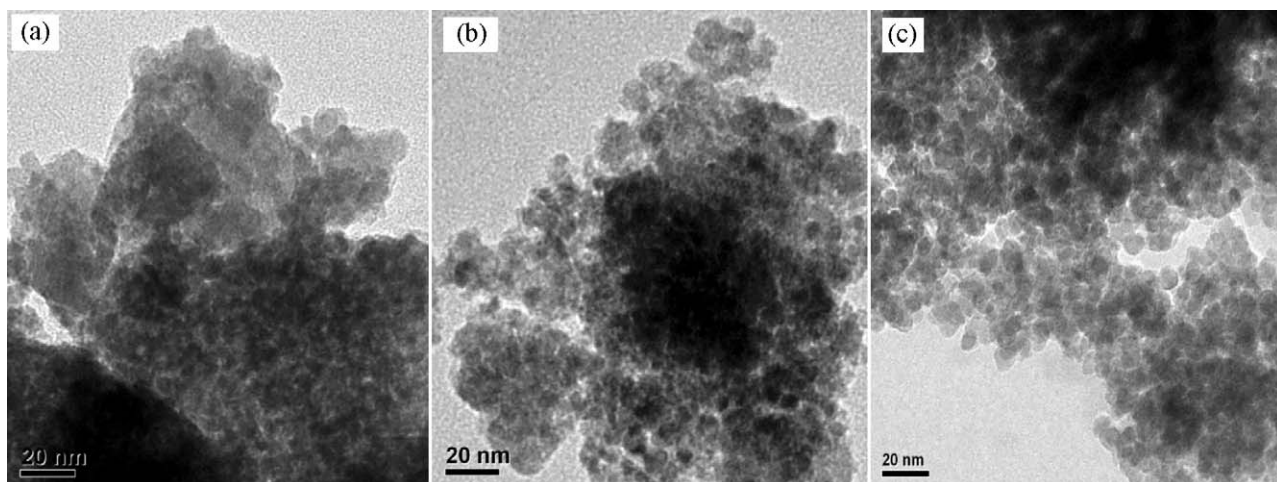


Fig. 5. Transmission electron microscopy (TEM) images of (a) CZL1, (b) CZL2 and (c) CZL3.

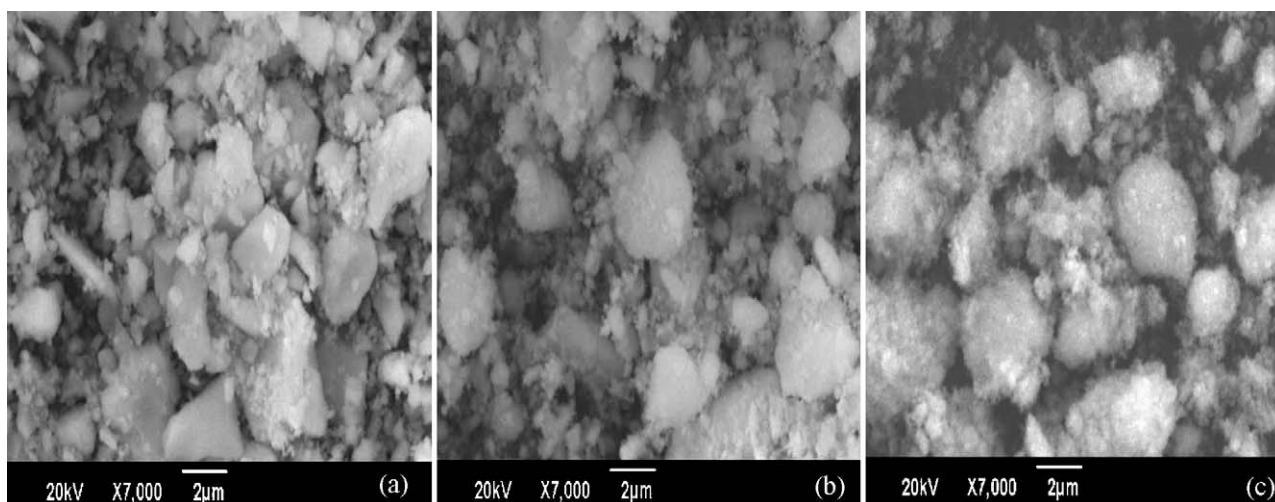


Fig. 6. Scanning electron micrographs of (a) CZL1, (b) CZL2, and (c) CZL3 calcined at 500 °C.

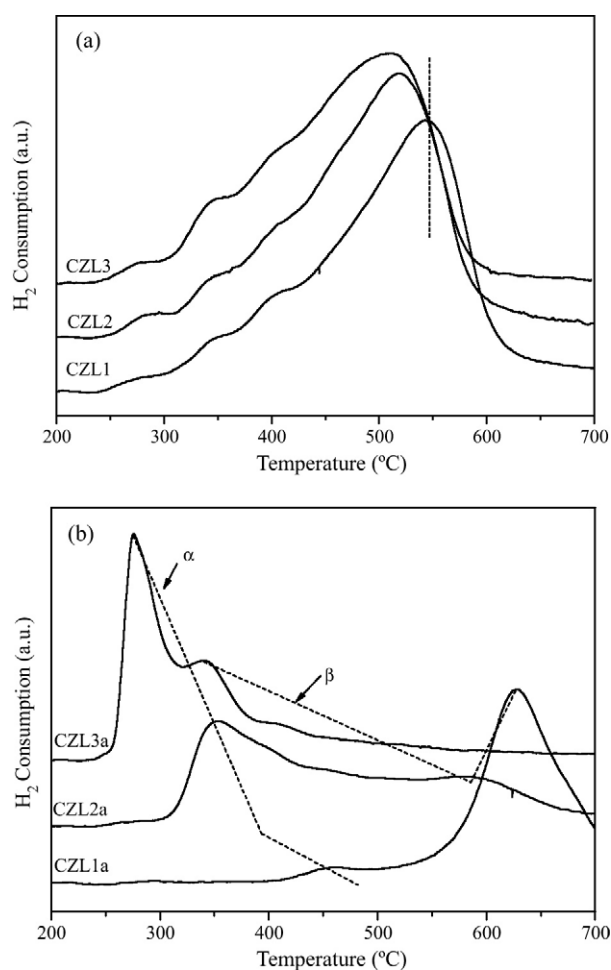


Fig. 7. TPR traces for the fresh (a) and aged (b) supports.

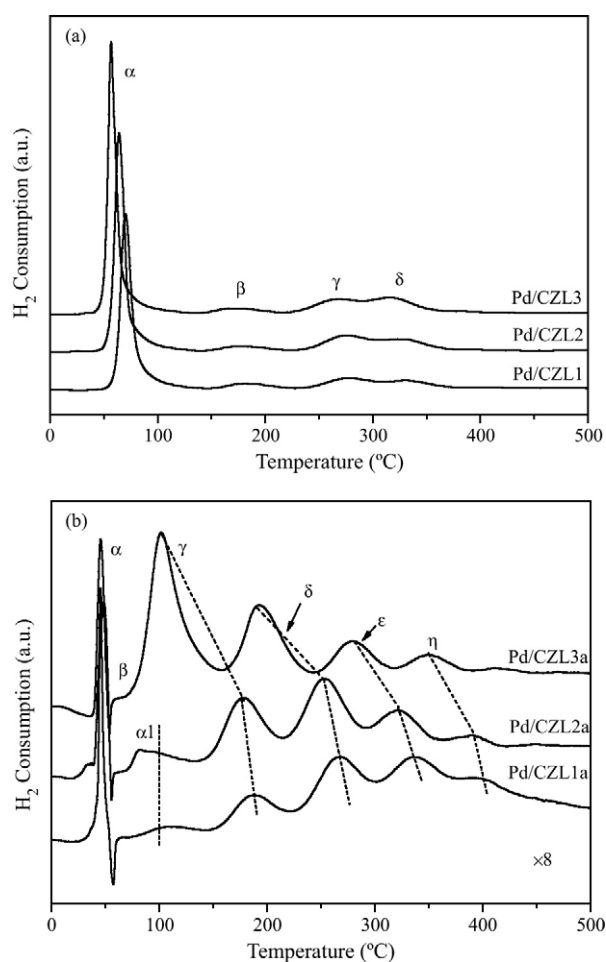
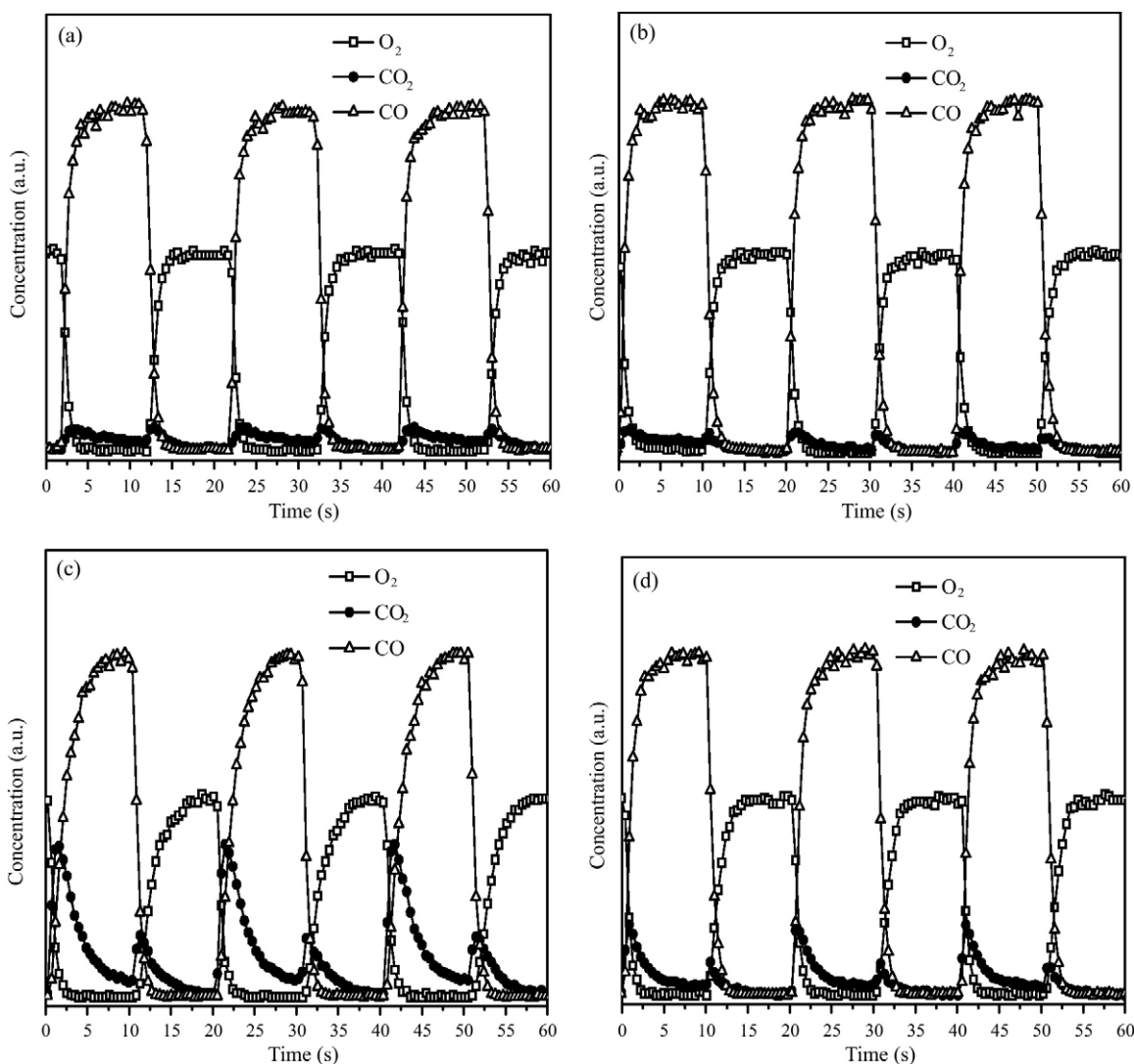


Fig. 8. TPR traces for the fresh (a) and aged (b) catalysts.

(0.1%)–NO<sub>2</sub> (0.03%)–C<sub>3</sub>H<sub>6</sub> (0.067%)–C<sub>3</sub>H<sub>8</sub> (0.033%)–CO (0.75%)–O<sub>2</sub> (0.745%) with balance Ar at a GHSV of 43,000 h<sup>−1</sup> referred to the catalyst volume and to a gas flow rate at room temperature (25 °C). The contents of CO, NO, NO<sub>2</sub> and total HC (C<sub>3</sub>H<sub>6</sub> and C<sub>3</sub>H<sub>8</sub>) were recorded by a Bruker EQ55 FTIR spectrometer coupled with a multiple reflection transmission cell (Infrared Analysis Inc.) before and

after the simulated gas passed the reactor. The air/fuel ratio ( $\lambda$ ) is defined as  $\lambda = (2V_{O_2} + V_{NO} + 2V_{NO_2}) / (V_{CO} + 9V_{C_3H_6} + 10V_{C_3H_8})$  ( $V$  means concentration in volume percent unit),  $\lambda = 1$  was utilized in all the activity measurements and the air/fuel ratio experiment was carried out at 400 °C with adjusting the concentration of O<sub>2</sub>.



**Fig. 9.** Representative transition curve with alternate dynamic pulses of 4% CO/1% Ar/He (10 s) and 2% O<sub>2</sub>/1% Ar/He (10 s) under 0.05 Hz: (a) CZL3; (b) CZL3a; (c) Pd/CZL3; (d) Pd/CZL3a.

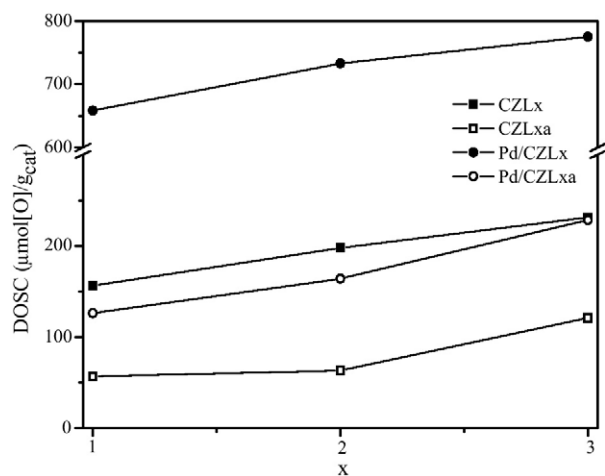


**Fig. 10.** DOSC of CZLx, CZLxa, Pd/CZLx, and Pd/CZLxa series samples ( $x = 1, 2$ , and  $3$ ) with dynamic pulses of 4% CO/1% Ar/He and 2% O<sub>2</sub>/1% Ar/He under 0.05 Hz.

### 2.3. Characterization techniques

Powder X-ray diffraction (XRD) patterns were recorded by an ARL X'TRA diffractometer using nickel-filtered Cu K $\alpha$  radiation operating at 40 kV and 40 mA and with 0.02° step size scanning from 20° to 80° ( $2\theta$ ). Small-angle XRD data were collected on a RigakuD/max-3BX X-ray diffractometer, and the range of scan was  $2\theta = 1\text{--}10^\circ$ .

The nitrogen adsorption/desorption isotherms, BET surface areas and pore size distribution of the samples were determined by nitrogen physisorption at 77 K using a Coulter OMNISORP-100 apparatus, after degassing the samples in vacuum ( $<10^{-5}$  Torr) at 200 °C for 2 h.

Scanning electron microscopy (SEM) observation was carried out using a JEOL JSM-6390A analytical scanning electron microscope operating at an acceleration voltage of 20 kV. The samples were prepared by sprinkling the powder oxides onto double-sided sticky tape and mounted on a microscope stub without any further treatment.

Transmission electron microscopy (TEM) examinations were conducted using a JEOL JEM-2010 electron microscope operating at 200 kV. Portions of samples were crushed in an agate mortar and suspended in ethanol. After ultrasonic dispersion, a droplet was

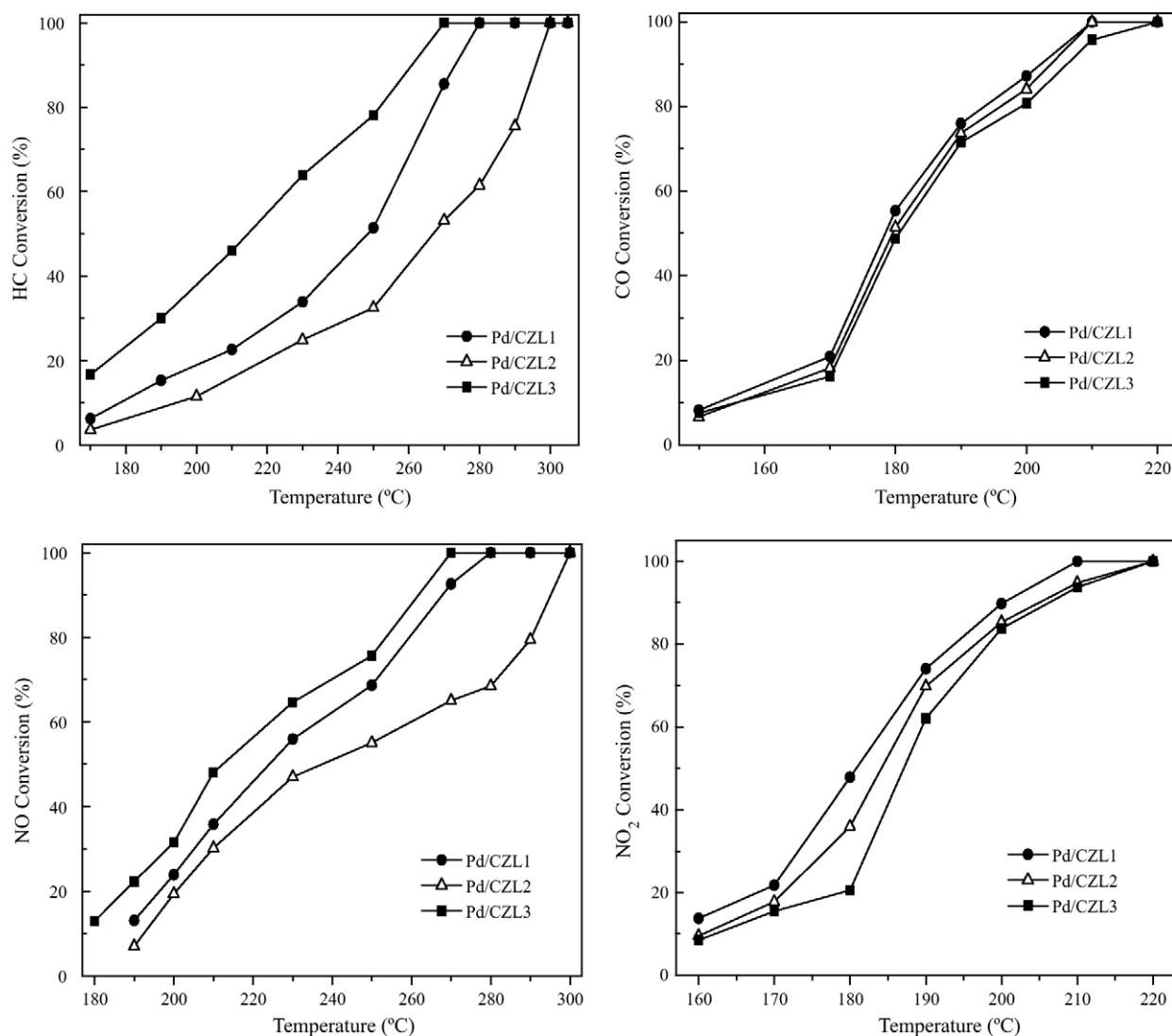


Fig. 11. Light-off curves of HC, CO, NO, and NO<sub>2</sub> at stoichiometry ( $\lambda = 1$ ) over the fresh catalysts.

deposited on a copper grid supporting a perforated carbon film. Bright-field micrographs were recorded over selected areas.

X-ray photoelectron spectroscopy (XPS) analysis was performed on a PHI5000c spectrometer with the Mg K $\alpha$  radiation (1253.6 eV) operating at 14 kV and 20 mA. The binding energies are calibrated with the C<sub>1s</sub> level of adventitious carbon (284.6 eV) as the internal standard reference.

Temperature programmed reduction (TPR) measurements were carried out on a GC-1690 chromatography to observe the reducibility of the catalysts. Prior to H<sub>2</sub>-TPR measurement, 50 mg catalyst was pretreated at 300 °C in air for 0.5 h. The reducing gas was a mixture of 5 vol.% H<sub>2</sub> in Ar (40 ml/min), which was purified using deoxidizer and silica gel. The experimental temperature was raised at a constant rate of 10 °C/min. The consumption of hydrogen during the reduction was measured by a thermal conductivity detector (TCD), and the water formed during H<sub>2</sub>-TPR was absorbed with 5A molecular sieve.

The dynamic oxygen storage capacity (DOSC) measurements with CO–O<sub>2</sub> pulse were applied at 400 °C. CO (4% CO/1% Ar/He at 300 ml/min for 10 s) and O<sub>2</sub> (2% O<sub>2</sub>/1% Ar/He at 300 ml/min for 10 s) streams were pulsed alternatively with a pulsation frequency (i.e., the number of times CO–O<sub>2</sub> pulse was performed per second) of 0.05 Hz. The DOSC value was obtained by integrating the

CO<sub>2</sub> formed during one CO–O<sub>2</sub> cycle and was expressed as  $\mu\text{mol [O]}/\text{g}$ .

### 3. Results and discussion

#### 3.1. Textual and structural characterization

##### 3.1.1. XRD

The X-ray diffraction patterns of the fresh and aged supports are depicted in Fig. 1. The lattice parameters derived from a Rietveld refinement of XRD results and the crystal size calculated according to Scherrer equation are summarized in Table 1. As shown in Fig. 1a, the reflections are quite broad and symmetrical for all the fresh CZLx

Table 1

Lattice parameters and crystallite size determined by XRD for all the supports.

Samples	Lattice constants ( $\text{\AA}$ )	Crystallite size ( $\text{\AA}$ )
CZL1	$a = 3.655, c = 5.256$	6.4
CZL2	$a = 3.675, c = 5.216$	6.0
CZL3	$a = 3.661, c = 5.228$	5.8
CZL1a	$a = 3.627, c = 5.224$	25.3
CZL2a	$a = 3.628, c = 5.230$	25.0
CZL3a	$a = 3.644, c = 5.232$	20.4

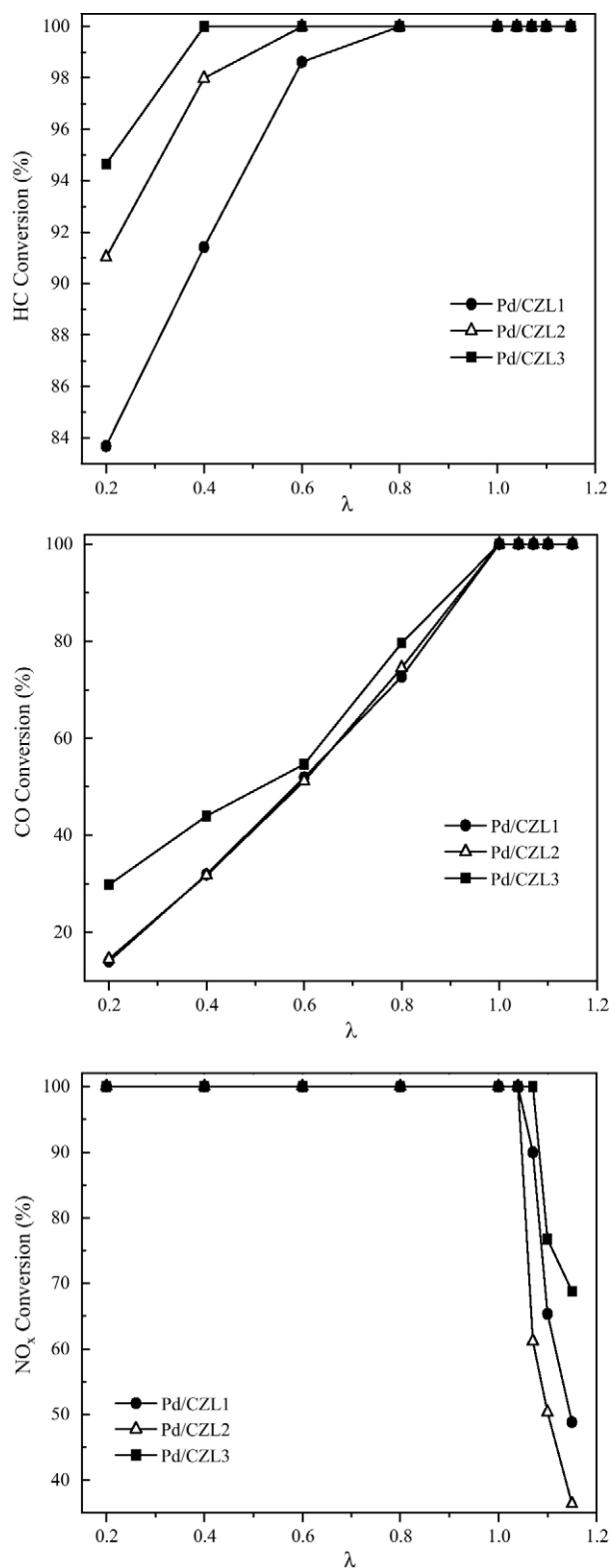


Fig. 12. Conversion curves of HC, CO and NO<sub>x</sub> as a function of air/fuel ratio ( $\lambda$ ) over the fresh catalysts.

samples, indicating the formation of fine nanostructure [9]. The XRD diffraction peaks of all the fresh samples appear to be consistent with tetragonal ceria–zirconia solid solution (space group  $P4_2/nmcs$ ,  $Z=2$ , ICSD No. 68590), and no peak splitting that would indicate the presence of two phases could be detected. Furthermore, extra reflections due to non-incorporated La<sub>2</sub>O<sub>3</sub> are absent

in any XRD patterns of fresh CZLx mixed oxides. Most importantly, Table 1 shows that the lattice parameter for all the La doped samples is larger than that of CZ ( $a=3.625$ ;  $c=5.218$ ) reported in our previous work [23], indicating the expansion of lattice parameter due to the insertion of La into ceria–zirconia tetragonal lattice. Based on the discussion presented above, the formation of tetragonal Ce–Zr–La solid solution could be proved.

After calcination at 1100 °C for 4 h, the diffraction peaks experience a sharpening, indicating a significant sintering of the CZL solid solution. More characteristic diffraction peaks assigned to tetragonal CZL solid solution appear, resulting from the growth and integrity of crystal grain. From Table 1, it can be seen that CZL3 shows the smallest particle size among all the fresh samples. Moreover, CZL3a also possesses relatively smaller grain size compared with CZL1a and CZL2a, which indicates that sample prepared by supercritical drying method exhibits better thermal stability.

What should be mentioned is that, two small shoulder peaks at 48.7° and 57.9° (marked as pentagram) appear in the case of CZL1a and CZL2a compared with CZL1 and CZL2. These two additional peaks are consistent with neither tetragonal CZL solid solution nor hexagonal La<sub>2</sub>O<sub>3</sub>. According to literature [2,43], the appearance of these small peaks is due to the arrangement of the cations induced by high temperature treatment. The most possible explanation could be put forward as that these peaks are associated with the portion of deteriorated Ce–Zr–La mixed oxide separated from the solid solution owing to the high temperature treatment. The absence of the two shoulder peaks for CZL3a indicates that the CZL solid solution prepared by supercritical drying method exhibits higher thermal stability and structural homogeneity than samples prepared by the usual drying method.

In order to give more light to the structure, small-angle XRD characterization of the fresh CZL1, CZL2, and CZL3 was carried out, and the obtained patterns were displayed in Fig. 2. CZL1 shows a weak and broad peak in the range of  $2\theta=2-6^\circ$ , revealing the formation of long-range ordered nanostructure [44]. According to literature [45], the small peaks at lower angle could be ascribed to the partly ordered mesopores and/or the uniform shape and size of the “building block” nano-particles. For CZL1, a faint peak at  $2\theta \sim 1.5^\circ$  can be observed, which indicates a spot of mesopores in CZL1. With regard to CZL2 and CZL3, there are several strong and well-resolved peaks in the small range ( $2\theta=0.8-2^\circ$ ), and the intensity for the peak at  $2\theta \sim 1.5^\circ$  is relatively high, indicating the existence of distinct mesostructure.

### 3.1.2. N<sub>2</sub> adsorption measurement

Table 2 gives values of the specific area calculated according to the BET method and the mean pore size estimated from desorption branch of the isotherm by the BJH method, as well as the cumulative pore volume. The nitrogen adsorption/desorption isotherms for fresh supports are shown in Fig. 3.

As it can be seen in Table 2, CZL3 shows the highest BET surface area and cumulative pore volume among all the fresh samples. The pore volume of CZL3 is even ten times as large as that of CZL1. This observation indicates that the supercritical drying could eliminate the vapor–liquid interface, leading to the conservation of porous structure [46]. Moreover, the specific surface area of CZL2 is higher than that of CZL1. In order to understand these differences, we should know what happens in the drying process. When the precipitation of the gel is carried out, particles are formed and linked together through molecular water hydrogen bonded to the surface OH<sup>−</sup> groups [47]. The presence of water is the main resource for the capillary force at the vapor–liquid interface, and the substitution of water by ethanol leads to the decrease of surface tension, which prevents the occurrence of agglomeration to some extent. The substitution would be radical due to the adoption of ethanol supercritical drying, in which the vapor–liquid interface



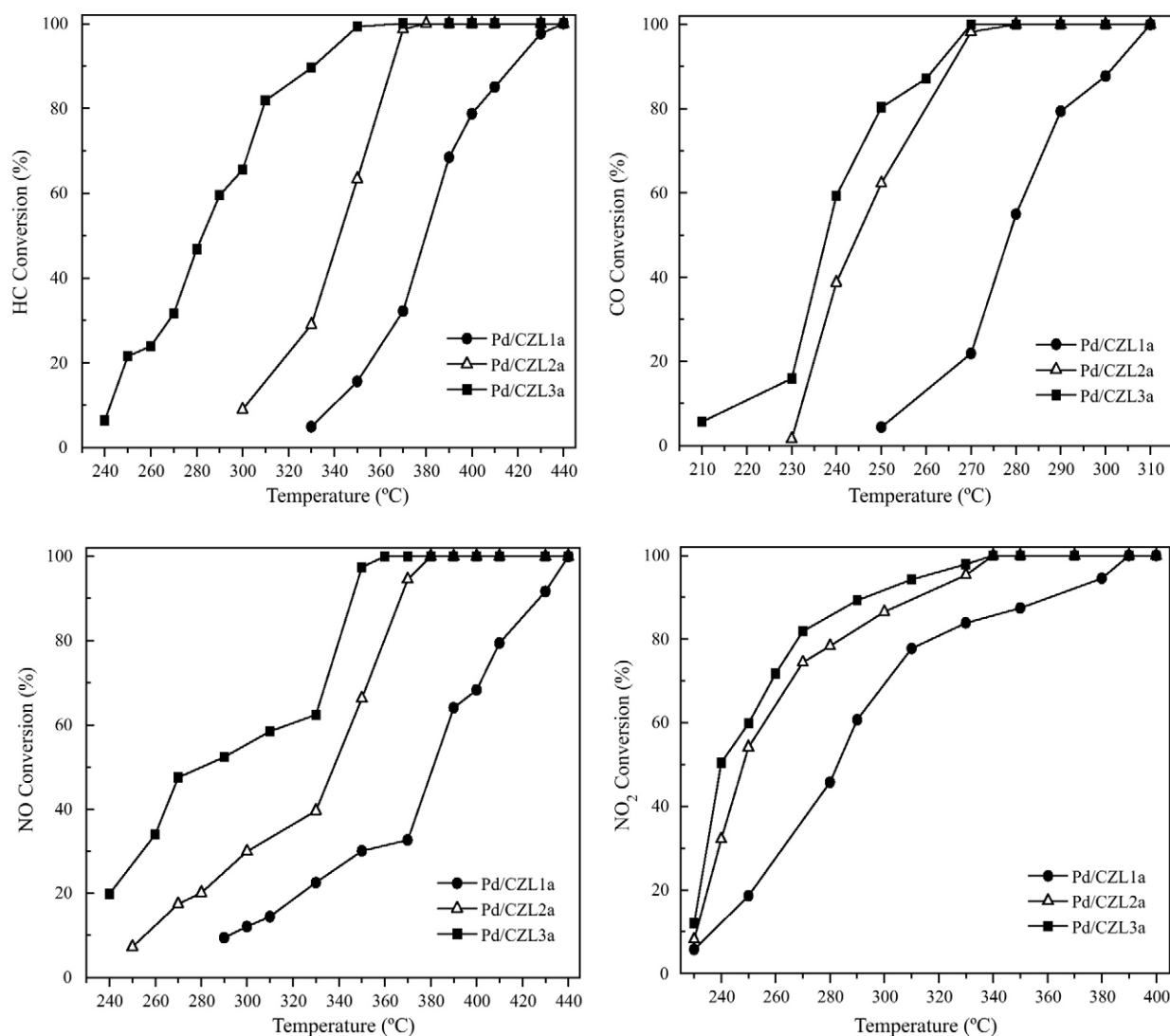


Fig. 13. Light-off curves of HC, CO, NO, and NO<sub>2</sub> at stoichiometry ( $\lambda = 1$ ) over the aged catalysts.

disappears. After aging at 1100 °C for 4 h, all of the investigated samples show a considerable structural shrinkage, manifested by the dramatic decrease of specific surface area and the absence of micro-pore volume. The high temperature treatment is believed to be the main reason for the loss of elementary pores on the pore walls [48]. However, CZL3a maintains higher surface area and larger pore volume after aging compared with CZL1a and CZL2a, the pore structure of which have been collapsed entirely, indicating the good thermal stability of CZL3 prepared by supercritical drying method.

The comparison of isotherms reported in Fig. 3 shows a significant and progressive modification going from CZL1 to CZL3. The adsorption-desorption isotherm of CZL1 exhibits a typical reversible type IV curve (IUPAC classification) without hysteresis loops, and no clear capillary condensation step can be observed

in the range of relative pressure ( $P/P_0 = 0.0-1.0$ ). This observation implies that CZL1 has a low incidence of pores [44], as evidenced by the low cumulative pore volume in Table 2, resulting from the quick contraction in the process of drying in the oven. Type IV isotherm with type H2 hysteresis loop is recorded for CZL2 which indicates the presence of mesoporous texture [49–51], ink-bottle shaped pore in detail [52]. The formation of ink-bottle structure is due to the substitution of water by ethanol. The ethanol at the external surface evaporates more easily, resulting in the shrinkage of surface structure, and forming the pores which the pore body is larger than pore mouth. The isotherm of CZL3 conforms to type IV with a type H1 hysteresis loop, arising from the formation of large interparticle mesopores both at the external surface and in the inner region of the agglomerate [53],

**Table 2**  
Surface area, pore volume and mean pore diameter of all the supports.

Sample	$S_{\text{BET}}$ (m <sup>2</sup> /g)	Cumulative pore volume (cm <sup>3</sup> /g)	$V_{\text{mic}}$ (cm <sup>3</sup> /g)	$V_{\text{mes}}$ (cm <sup>3</sup> /g)	$D_{\text{mic}}$ (nm)	$D_{\text{mes}}$ (nm)
CZL1	88.6	0.068	0.019	0.049	1.3	9.3
CZL2	120.7	0.147	0.035	0.112	1.3	7.2
CZL3	144.4	0.628	0.048	0.580	1.2	18.2
CZL1a	24.9	0.015	0.001	0.014	1.7	14.0
CZL2a	25.9	0.017	0.001	0.016	1.7	15.9
CZL3a	39.6	0.126	0.008	0.118	1.3	22.0



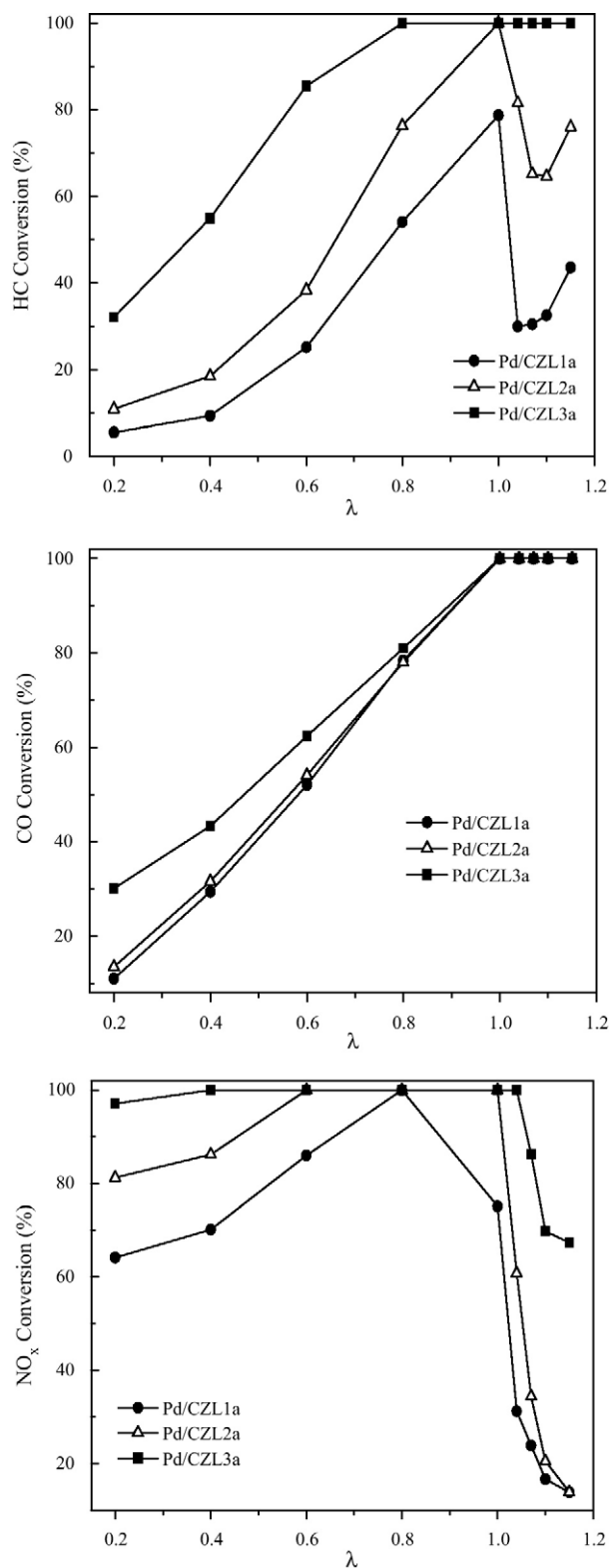


Fig. 14. Conversion curves of HC, CO and  $\text{NO}_x$  as a function of air/fuel ratio ( $\lambda$ ) over the aged catalysts.

which are generally reported for the existence of cylindrical pores [52].

The change in the isotherm/hysteresis due to the different drying method is associated with a shift in the pore size distribution to higher pore diameter as shown in Fig. 4. From Fig. 4a, it can be seen that CZL3 shows a wide pore size distribution apparently

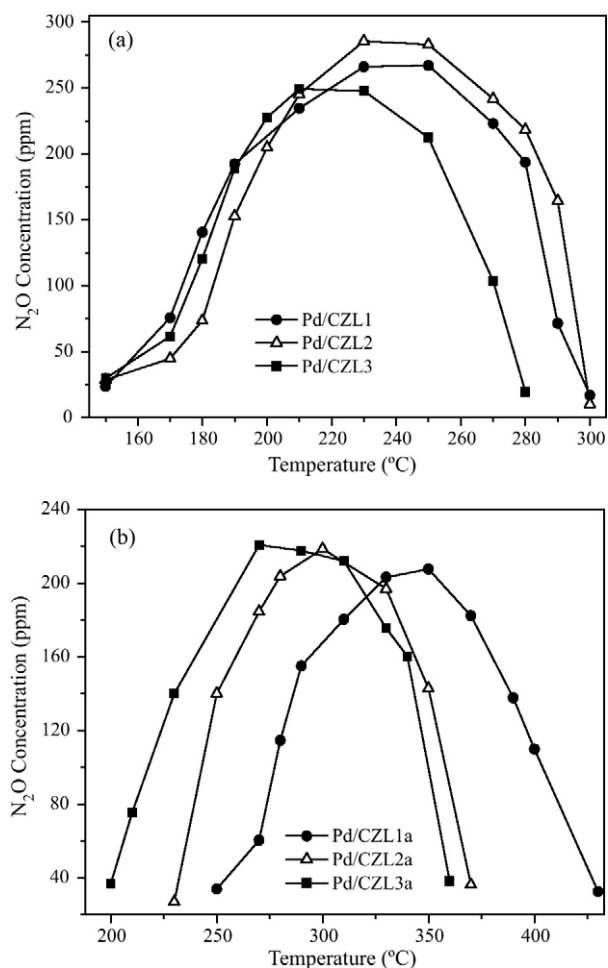


Fig. 15. Influence of the reaction temperature on the formation of  $\text{N}_2\text{O}$  over fresh (a) and aged (b) catalysts.

(4–70 nm). In the actual process of catalytic conversion, the wide pore size distribution and porosity of the catalyst is beneficial to the adsorption/desorption of target pollutant, resulting in higher catalytic activity [23]. For the aged samples, Fig. 4b shows that the pore structure of CZL1a and CZL2a is destroyed entirely, and no pore size distribution could be detected. However, CZL3a still exhibits the wide pore size distribution although the pore structure is wrecked to some extent.

### 3.1.3. Morphology analysis

To explore the structural evolution at atomic scale, studies by transmission electron microscope (TEM) were performed on all of the fresh CZLx samples, and the obtained micrographs are shown in Fig. 5. The images show that all the samples are composed of many sphere-like nanoclusters. At the same time, these primary particles of CZLx around 4–5 nm have agglomerated and the dense secondary particles are observed. The differences in the drying process result in some influence on the morphology of the obtained CZLx. Focusing on Fig. 5a, massive particles and compact agglomeration are observed apparently, indicating the inferior textural homogeneity of CZL1. The images shown in Fig. 5b and c reveal that the clusters for CZL2 and CZL3 are of narrow size distribution and more regular shape. Moreover, the clusters in the case of CZL3 are of loosely accumulated.

Scanning electron micrographs of three fresh CZLx samples are reported in Fig. 6. The larger particle sizes displayed in the SEM images compared with the crystallite sizes measured by XRD illus-

trates that powder particles are reunited to some extent, which agrees well with the TEM results. Therefore, it can be concluded that the pores are created from CZLx nano-particles when they are agglomerated, and the interstitial space between nano-particles in the agglomeration might act as pores [54]. That is why the samples have a wide pore size distribution as shown in Fig. 4. A distinct difference in the microstructure among the three fresh samples could be observed from Fig. 6. For CZL1, the slab-shaped particles accumulated tightly with small and irregular pore size owing to the intensive constriction in the process of usual drying technology. As a result of the replacement of water by ethanol in the CZL2 colloid, the compaction of the micelle is minor, and the edge of the agglomerated particles is coarsely. Fluffy particles with subsphaeroidal shape are exhibited in the case of CZL3, and the pores between particles are apparent. The loose accumulation and distinct porosity are main reasons to cause the high BET surface area. The literature have reported that the higher is the surface area, the larger the number of surface sites the sample can provide, and thus the better the catalytic activities the sample will have [55,56].

### 3.1.4. XPS

An XPS investigation was conducted to explore the distribution of the elements on the surface. The surface elemental compositions of the catalysts calculated from the normalized peak areas of the Ce 3d, Zr 3d, La 3d, Pd 3d and O 1s core level spectra are shown in Table 3.

Recent XPS study reported that the binding energies of PdO and metallic Pd<sup>0</sup> are ca. 336.8 and 335.2 eV, respectively [57–59]. However, no distinct Pd 3d spectra are observed in the case of both fresh and aged catalysts due to two influencing factors. One is the extremely low Pd loading content which approaches the limit detection, and the other is the overlapping by the strong Zr 3P spectra for Zr-rich in the composition.

Table 3 shows that the surface content of Ce element and concentration of Ce<sup>3+</sup> in Ce increases in the sequence of Pd/CZL3 > Pd/CZL2 > Pd/CZL1. As reported in literature [60], the presence of Ce<sup>3+</sup> is associated with the formation of oxygen vacancy, which is the main factor that influences the oxygen mobility and the result that Pd/CZL3 shows the highest dynamic oxygen storage capacity is understandable.

The aging induced effects are clearly seen comparing the XPS data of aged catalysts with that of the fresh ones. From Table 3, it can be seen that the surface content of La increases significantly after aging, arising from the migration of La from bulk to surface caused by high temperature treatment. On the contrary, the surface content of Ce and Zr decrease, and the ratio of Zr/Ce is higher than the theoretical value for all the aged samples, indicating the sintering of samples. The results presented above demonstrate that the structure homogeneity is deteriorated severely in the process of thermal treatment. What should be mentioned is that the surface content of Ce and concentration of Ce<sup>3+</sup> in Ce for Pd/CZL3a remains the highest. That is why the DOSC of Pd/CZL3a is higher than that of the other aged samples (as shown in Fig. 10). At the same time, the surface content of La is the lowest, and the ratio of Zr/Ce is the nearest to the theoretical value, indicating the relatively higher thermal stability of Pd/CZL3.

### 3.2. Redox behavior

Fig. 7 shows the hydrogen uptakes as a function of temperature obtained for the fresh and aged supports. The TPR profiles of all the fresh samples (shown in Fig. 7a) feature one dominant broad peak with maximum at 510–550 °C, which is attributed to the surface/bulk reduction of the support [15,61–63]. The observation that the surface and bulk reduction is not distinguished clearly on the fresh supports implies that the CZL solid solution exhibits

good redox property [41]. The peak maximum shifts toward lower temperature from CZL1 to CZL3 apparently, indicating that the supercritical synthesis can provide the CZL solid solution with better reducibility [64].

After aging, some interesting differences in redox properties between fresh and aged supports can be observed. For all the aged samples, an additional reduction peak appears compared with the H<sub>2</sub>-TPR profile of the fresh support. The peak centered at the relatively lower temperature is designated as peak  $\alpha$ , and the other one is labeled as peak  $\beta$ , which are generally ascribed to the reduction of surface and sub-surface oxygen [65–67]. However, only slight H<sub>2</sub> consumption decrease is measured after aged for the supports. For CZL1, CZL2 and CZL3, the total H<sub>2</sub> consumption is 542.7, 544.9 and 595.2  $\mu\text{mol/g}_{\text{cat}}$ , respectively. In addition, the total H<sub>2</sub> consumption for the corresponding aged samples is 472.3, 522.9 and 544.0  $\mu\text{mol/g}_{\text{cat}}$ , respectively. This observation indicates that the contribution of bulk reduction should not be ignored for the aged supports. In the case of CZL1a, there is an increase of the peak temperature by about 80 °C when comparing with CZL1, suggesting that the redox behavior of CZL1 is destroyed resulting from the high temperature treatment. With regard to CZL3a, the peak temperature for both peak  $\alpha$  and  $\beta$  is the lowest among all the aged support, indicating the superior redox properties of CZL3a.

From the analysis mentioned above, it could be assured that CZL3 prepared by the supercritical synthesis has a higher redox property than that prepared by the common drying method, especially for the samples aged at high temperature.

H<sub>2</sub>-TPR profiles of the fresh and aged catalysts are presented in Fig. 8. All of the fresh catalysts feature a sharp reduction peak with the maximum in the temperature of 55–70 °C (peak  $\alpha$ ), which is attributed to the reduction of finely dispersed PdO particles [68,69]. The temperature of peak  $\alpha$  increases in the following sequence: Pd/CZL3 < Pd/CZL2 < Pd/CZL1, which indicates the higher reducibility of Pd/CZL3 compared with the others. Combined with the analysis of the support, we can conclude that three tiny peaks (peak  $\beta$ ,  $\gamma$  and  $\delta$ ) in the range of 150–350 °C are also associated with the reduction of surface oxygen, which can be assigned to the reduction of surface/subsurface crystallites with different particle sizes in detail [38,68]. Based on the amount of H<sub>2</sub> consumption observed over a standard CuO sample in similar TPR procedures, it is noticed that the total amount of the H<sub>2</sub> consumption for peak  $\alpha$  is too large to be reasonably attributed to the reduction of noble metal oxides absolutely, indicating the back-spillover of the oxygen process from the support to the PdO surface [70,71]. For instance, the H<sub>2</sub> consumption for theoretical PdO is just 41  $\mu\text{mol/g}_{\text{cat}}$ , while that for peak  $\alpha$  in the case of Pd/CZL3 is 887  $\mu\text{mol/g}_{\text{cat}}$ . In the other words, there is a strong metal-support interaction between the support and active noble metal. The reduction peak temperature for both PdO and surface oxygen with regard to Pd/CZL3 is the lowest among all the fresh catalysts, proving that Pd/CZL3 exhibits the optimum redox behavior due to the strong interaction between PdO and CZL3.

After aging, the intensity of peak  $\alpha$  decreases obviously due to the presence of Pd induced by pyrolysis and the agglomeration of PdO particles. Therefore, the additional negative peak at ca. 60 °C (peak  $\beta$  in Fig. 8b) is attributed to the decomposition of palladium hydride formed when reduced Pd is exposed to H<sub>2</sub> furthermore [72]. In the case of Pd/CZL1a and Pd/CZL2a, a weak peak centered at ca. 100 °C is observed (peak  $\alpha_1$ ), which is related to the reduction of stable PdO formed on the interaction between PdO and the support [59]. The absence of peak  $\alpha_1$  in Pd/CZL3a is due to the overlap by peak  $\gamma$ . Peak  $\gamma$ ,  $\delta$ ,  $\epsilon$  and  $\eta$  are also associated with the reduction of surface/subsurface crystallites with different particle sizes. The appearance of more reduction peak of surface/subsurface oxygen (compare with the fresh catalyst) is attributed to the decline of homogeneity in grain size resulting from the sintering of sam-

**Table 3**  
Surface composition and surface atom ratio in the fresh and aged catalysts derived from XPS analyses.

Sample	Surface composition (at.%)					Zr/Ce	Ce <sup>3+</sup> 3d <sub>5/2</sub> in Ce (%)
	Ce 3d	Zr 3d	La 3d	Pd 3d	O 1s		
Pd/CZL1	3.60	14.46	0.76	–	81.18	4.02	16.2
Pd/CZL2	3.99	15.86	0.92	–	79.24	3.97	17.6
Pd/CZL3	5.42	16.50	1.30	–	76.78	3.04	19.8
Pd/CZL1a	2.73	13.47	2.24	–	81.56	4.93	16.1
Pd/CZL2a	2.84	13.56	2.15	–	81.45	4.77	17.4
Pd/CZL3a	3.52	14.67	2.11	–	79.70	4.17	18.9

ples. Similarly, for the fresh catalysts, all of the reduction peaks for Pd/CZL3a show the lowest temperature among the aged catalysts, no matter the reduction peak of PdO or the reduction peak of the support, which implies that Pd/CZL3a exhibits good redox properties due to the good thermal stability of the corresponding support.

### 3.3. Dynamic oxygen storage capacity measurement

The representative evolution curves of CO, O<sub>2</sub> and CO<sub>2</sub> during the process of alternative dynamic pulse of 4% CO/1% Ar/He and 2% O<sub>2</sub>/1% Ar/He under 0.05 Hz over CZL3, CZL3a, Pd/CZL3 and Pd/CZL3a are shown in Fig. 9, where only three CO–O<sub>2</sub> cycle is selected from the continuous transient CO–O<sub>2</sub> pulses to represent the dynamic OSC curve. The experimental temperature is 400 °C. The behavior of bimodal CO<sub>2</sub> curves under single CO–O<sub>2</sub> cycle is in good agreement with the results described in other research [67,69,73–75]. The CO<sub>2</sub> peak appears at the start of the CO pulse is designated as CO<sub>2</sub> (1) and the second peak is labeled as CO<sub>2</sub> (2).

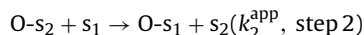
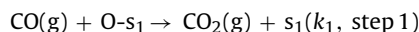
According to Descorme et al. [73] and Boaro et al. [74], the coexistence of CO and gaseous O<sub>2</sub> should be taken into the analysis of CO<sub>2</sub> concentration curves. In the case of CO<sub>2</sub> (1), since the catalyst is partially oxidized before the introduction of CO, the CO<sub>2</sub> formation included CO<sub>2</sub> generating from both the catalytic oxidation of CO in the presence of gaseous oxygen and the oxygen release reaction. Christou et al. [70] have developed a two-step Eley-Rideal (E-R) reaction mechanism that involves the reaction of gaseous CO with the oxygen species of PdO and of the back-spillover of oxygen form oxygen storage material to the oxygen vacant sites of surface PdO. The formation of CO<sub>2</sub> (2) is completely attributed to the catalytic oxidation of CO since the oxides are partially reduced at this moment. Fan et al. [4] confirmed the existence of catalytic oxidation of CO by gaseous O<sub>2</sub> via comparing the CO step in CO–O<sub>2</sub> cycles and the first pulse in the successive CO pulse measurement. Meanwhile, the effect of carbonate formation is proposed after in situ DRIFTS inspection of the reactions during the CO–O<sub>2</sub> cycles. To sum up, CO oxidation by mixed oxides and gaseous oxygen, carbonate formation and decomposition are all responsible for the bimodal profiles of CO<sub>2</sub> in DOSC test.

**Table 4**  
Light-off (*T*<sub>50%</sub>) and full-conversion (*T*<sub>90%</sub>) temperature of HC, CO, NO, and NO<sub>2</sub> over the fresh and aged catalysts.

Catalyst	<i>T</i> <sub>50%</sub> (°C)				<i>T</i> <sub>90%</sub> (°C)			
	HC	CO	NO	NO <sub>2</sub>	HC	CO	NO	NO <sub>2</sub>
Pd/CZL1	249	178	224	181	273	202	268	200
Pd/CZL1a	380	278	381	283	417	302	427	361
Δ <i>T</i> <sub>50%</sub> , Δ <i>T</i> <sub>90%</sub>	131	100	157	102	144	100	159	161
Pd/CZL2	267	179	238	181	296	204	295	205
Pd/CZL2a	343	245	337	248	365	265	366	311
Δ <i>T</i> <sub>50%</sub> , Δ <i>T</i> <sub>90%</sub>	75	66	99	64	69	61	71	105
Pd/CZL3	214	181	212	187	261	206	262	202
Pd/CZL3a	283	238	279	240	331	263	346	294
Δ <i>T</i> <sub>50%</sub> , Δ <i>T</i> <sub>90%</sub>	69	57	67	53	70	57	84	88

Δ*T*<sub>50%</sub> = *T*<sub>50%</sub> (aged catalyst) – *T*<sub>50%</sub> (fresh catalyst); Δ*T*<sub>90%</sub> = *T*<sub>90%</sub> (aged catalyst) – *T*<sub>90%</sub> (fresh catalyst).

The DOSC values of CZLx, CZLax, Pd/CZLx and Pd/CZLxa (*x* = 1, 2, and 3) are presented in Fig. 10, and the DOSC amount is calculated by integrating the CO<sub>2</sub> formed with one CO–O<sub>2</sub> cycle. Agreeing well with the DOSC results for the supports, the DOSC values for the corresponding catalysts follow the sequence of Pd/CZL3 > Pd/CZL2 > Pd/CZL1, which also occurs for the aged samples. This observation indicates that the samples prepared by supercritical drying method exhibit higher DOSC than those prepared by usual drying method. The E-R mechanism is based on the following two mechanistic steps:



where *s*<sub>1</sub> denotes an oxygen vacant adsorption site on the PdO surface, *s*<sub>2</sub> denotes a site on support where an adsorbed oxygen and/or lattice oxygen species is associated with, *k*<sub>1</sub> is the intrinsic rate constant of elementary step 1 (CO oxidation reaction), and *k*<sub>2</sub><sup>app</sup> is an apparent rate constant associated with the kinetics of the back-spillover of oxygen process from support to the surface of PdO [71]. Combined with the fact (shown in Fig. 10) that the DOSC is enhanced obviously after Pd loading, we can conclude that there is a strong and fast back-spillover effect from support to active PdO species. A severe loss of DOSC is obtained with increasing calcination temperature from 500 to 1100 °C for both supports and catalysts due to the sintering effect which result in the deteriorated structure of the support and the agglomeration of highly dispersed PdO.

### 3.4. Catalytic activity results

Fig. 11 presents the activity profiles of HC, CO, NO and NO<sub>2</sub> under stoichiometric reaction conditions over Pd/CZLx catalysts calcined at 500 °C. In the light off test for HC and NO conversion, a biggish increase of catalytic activity can be observed over Pd/CZL3. With regard to the conversion of CO and NO<sub>2</sub>, it appears that the differences between Pd/CZL1, Pd/CZL2, and Pd/CZL3 are very slight. Fig. 12 depicts the results of air/fuel (λ) test for the fresh catalysts. In our experiments, the conversions of HC, CO and NO<sub>x</sub> were tested

under different air/fuel ratios ( $\lambda = 0.2, 0.4, 0.6, 0.8, 1.0, 1.04, 1.07, 1.1$ , and  $1.15$ ). As shown in Fig. 12, the left side of the theoretical stoichiometric value ( $\lambda = 1$ ) is the lean oxygen, and the right is rich oxygen.  $W$  (the width of  $\lambda$  value) acts as another scale to evaluate the property of catalysts when HC, CO, and  $\text{NO}_x$  conversions all reach to 80% under rich and lean conditions. For example, the upper limit of the stoichiometric windows is limited by  $\text{NO}_x$  conversion under rich condition; the lower limit is limited by CO conversion under lean conditions for all samples. The upper limit subtracts the lower limit of  $\lambda$  is the value of  $W$ . A careful analysis of Fig. 12 reveals that the values of  $W$  for Pd/CZL1, Pd/CZL2, and Pd/CZL3 are 0.199, 0.244, and 0.290, respectively. Remarkably, Pd/CZL3 shows the widest operation window for the HC conversion, which is higher than 80% in the whole testing range, and reach 100% at  $\lambda = 0.4$ .

Fig. 13 presents the catalytic activities of Pd/CZL1a, Pd/CZL2a, and Pd/CZL3a as related to reaction temperature at  $\lambda = 1$ . An important point should be noted is that the catalytic activity for all of the four pollutants increased in the same order Pd/CZL1a < Pd/CZL2a < Pd/CZL3a, and the difference is obvious, indicating that Pd/CZL3a is more effective in the catalytic conversion of all the target pollutants. From Fig. 14, it can be known that after being aged at  $1100^\circ\text{C}$  for 4 h, the operation windows of all the catalysts are destroyed significantly except for Pd/CZL3a. For Pd/CZL1a, the HC conversion cannot reach 80% even at  $\lambda > 1.0$ , and the conversion approaches 80% only near the theoretical air/fuel ratio ( $\lambda = 1.0$ ) in the case of Pd/CZL2a. However, with regard to Pd/CZL3a, the HC conversion is higher than 80% at  $\lambda > 0.56$ . Moreover, the width of the operation window follows the same sequence as the catalytic activity for the aged catalysts.

What should be mentioned is that the formation of  $\text{N}_2\text{O}$  is also observed in the process of reaction, as shown in Fig. 15. From Fig. 15, it can be seen that the concentration of  $\text{N}_2\text{O}$  along with the reaction temperature displays parabola distribution. The preparation method affects the  $\text{N}_2\text{O}$  emission obviously. Fig. 15a shows that, there is no clear difference on the  $\text{N}_2\text{O}$  formation at the relatively lower temperature over the fresh catalysts. However, the concentration of  $\text{N}_2\text{O}$  decreases rapidly over Pd/CZL3 when the temperature is higher than  $230^\circ\text{C}$ , indicating that  $\text{N}_2\text{O}$  could be transformed in short order over Pd/CZL3. With regard to the aged catalysts, both the formation and the transformation of  $\text{N}_2\text{O}$  are rapid over Pd/CZL3a. In Section 3.1.2, we have proved that the support prepared by supercritical drying method exhibits remarkable porosity and wide pore size distribution, which is beneficial to the adsorption/desorption of pollutant in TWCs. That may be the main reason for the good catalytic activity of  $\text{N}_2\text{O}$  over Pd/CZL3 and Pd/CZL3a.

Table 4 summarizes the light-off temperature ( $T_{50\%}$ , the temperature at which 50% conversion is attained) and the full-conversion temperature ( $T_{90\%}$ , the temperature at which 90% conversion is attained) of HC, CO, NO and  $\text{NO}_2$  over all the fresh and aged catalysts. The difference between  $T_{50\%}$  and  $T_{90\%}$  of the aged catalyst and the corresponding fresh catalyst are labeled as  $\Delta T_{50\%}$  and  $\Delta T_{90\%}$ , respectively, which can be a measure of thermal stability of the catalysts. As shown in Table 4, in the case of Pd/CZL3 and Pd/CZL3a, the value of  $\Delta T_{50\%}$  and  $\Delta T_{90\%}$  for all the pollutants is the lowest among all the catalysts, indicating that Pd/CZL3 exhibits the best thermal stability.

Combined with the analysis presented above, it can be concluded that the Pd/CZL3 catalyst exhibits higher catalytic activity, wider operation window, as well as the better thermal stability even after aged at  $1100^\circ\text{C}$  for 4 h. The superior catalytic activity of Pd/CZL3 is related to its good redox behavior and the special structural/textural property of CZL3 result from the adoption of

supercritical drying method, which leads to the strong interaction between active metal and the support.

#### 4. Conclusion

Base on the results and discussion presented above, the following conclusions can be drawn: the structure/texture properties of CZL solid solution is affected by the drying method noticeably. Supercritical drying technology results in the absence of vapor–liquid interface in the drying process, which is accountable for the special mesopore structure of CZL3 with a wide pore size distribution. The superior behaviour of CZL3 is correlated to the enrichment of  $\text{Ce}^{3+}$  in the surface structure, the structural homogeneity and the special textural characteristics. Moreover, the corresponding supported Pd-only three-way catalyst also exhibits the relatively higher catalytic activity and wider operation air-to-fuel operation window.

#### Acknowledgements

We gratefully acknowledge the financial supports from the Ministry of Science and Technology of China (No: 2006AA060306, 2009AA064804).

#### References

- [1] H. Vidal, J. Kašpar, M. Pijolat, G. Colon, S. Bernal, A. Cordón, V. Perrichon, F. Fally, *Appl. Catal. B: Environ.* 27 (2000) 49.
- [2] Y. Nagai, T. Yamamoto, T. Tanaka, S. Yoshida, T. Nonaka, T. Okamoto, A. Suda, M. Sugiura, *Catal. Today* 74 (2002) 225.
- [3] A. Morikawa, T. Suzuki, T. Kanazawa, K. Kikuta, A. Suda, H. Shinjo, *Appl. Catal. B: Environ.* 78 (2008) 210.
- [4] J. Fan, D. Weng, X. Wu, X. Wu, R. Ran, J. Catal. 258 (2008) 177.
- [5] S.Y. Christou, H. Birgersson, A.M. Efstathiou, *Appl. Catal. B: Environ.* 71 (2007) 185.
- [6] A. Winkler, P. Dimopoulos, R. Hauer, C. Bach, M. Aguirre, *Appl. Catal. B: Environ.* 84 (2008) 162.
- [7] H. He, H.X. Dai, L.H. Ng, K.W. Wong, C.T. Au, *J. Catal.* 206 (2002) 1.
- [8] C. Larese, M. López Granados, R. Mariscal, J.L.G. Fierro, P.S. Lambrou, A.M. Efstathiou, *Appl. Catal. B: Environ.* 59 (2005) 13.
- [9] A. Papavasiliou, A. Tsetsekou, V. Matsouka, M. Konsolakis, I.V. Yentekakis, N. Boukos, *Appl. Catal. B: Environ.* 90 (2009) 162.
- [10] M. Ozawa, *J. Alloys Compd.* 275–277 (1998) 886.
- [11] X. Wu, L. Xu, D. Weng, *Appl. Surf. Sci.* 221 (2004) 375.
- [12] F. Dong, A. Suda, T. Tanabe, Y. Nagai, H. Sobukawa, H. Shinjo, M. Sugiura, C. Descorme, D. Duprez, *Catal. Today* 93–95 (2004) 827.
- [13] X. Wang, G. Lu, Y. Guo, Y. Xue, L. Jiang, Y. Guo, Z. Zhang, *Catal. Today* 126 (2007) 412.
- [14] A. Morikawa, K. Kikuta, A. Suda, H. Shinjo, *Appl. Catal. B: Environ.* 88 (2009) 542.
- [15] P. Fonasiero, R. Di Monte, G. Ranga Rao, J. Kašpar, S. Meriani, A. Trovarelli, M. Graziani, *J. Catal.* 151 (1995) 168.
- [16] M.V. Twigg, *Appl. Catal. B: Environ.* 70 (2007) 2.
- [17] L. Martín, J.L. Arranz, O. Prieto, R. Trujillano, M.J. Holgado, M.A. Galán, V. Rives, *Appl. Catal. B: Environ.* 44 (2003) 41.
- [18] N. Le Phuc, E.C. Corbos, X. Courtois, F. Can, P. Marecot, D. Duprez, *Appl. Catal. B: Environ.* 93 (2009) 12.
- [19] I. Heo, J. Choung, P. Kim, I. Nam, Y. Song, C. In, G. Yeo, *Appl. Catal. B: Environ.* 92 (2009) 114.
- [20] L.N. Ikryannikova, A.A. Aksenov, G.L. Markaryan, G.P. Murav'eva, B.G. Kostyuk, A.N. Kharlanov, E.V. Lunina, *Appl. Catal. A: Gen.* 210 (2001) 225.
- [21] X. Wu, X. Wu, Q. Liang, J. Fan, D. Weng, Z. Xie, S. Wei, *Solid State Sci.* 9 (2007) 636.
- [22] J.D. Lin, J.G. Duh, *Mater. Chem. Phys.* 78 (2002) 246.
- [23] Q. Wang, B. Zhao, G. Li, R. Zhou, *Environ. Sci. Technol.* 44 (2010) 3870.
- [24] T. Kobayashi, T. Yamada, K. Kayano, *Appl. Catal. B: Environ.* 30 (2001) 287.
- [25] B. Yue, R. Zhou, Y. Wang, X. Zheng, *J. Mol. Catal. A: Chem.* 238 (2005) 241.
- [26] B. Yue, R. Zhou, X. Zheng, W. Lu, *Fuel Process. Technol.* 89 (2008) 728.
- [27] X. Courtois, V. Perrichon, *Appl. Catal. B: Environ.* 57 (2005) 63.
- [28] V.R. Mastelaro, V. Briois, D.P.F. de Souza, C.L. Silva, *J. Eur. Ceram. Soc.* 23 (2003) 273.
- [29] E. Aneggi, C. de Leitenburg, G. Dolcetti, A. Trovarelli, *Catal. Today* 114 (2006) 40.
- [30] G. Li, B. Zhao, Q. Wang, R. Zhou, *Appl. Catal. B: Environ.* 97 (2010) 41.
- [31] G. Li, Q. Wang, B. Zhao, R. Zhou, *J. Mol. Catal. A: Chem.* 326 (2010) 69.
- [32] C. de Leitenburg, A. Trovarelli, F. Zamar, S. Maschio, G. Dolcetti, J. Llorca, *J. Chem. Soc., Chem. Commun.* (1995) 2181.

- [33] D. Terribile, A. Trovarelli, J. Llorca, C. de Leitenburg, G. Dolcetti, *Catal. Today* 43 (1998) 79.
- [34] J. Noh, O. Yang, D. Kim, S. Woo, *Catal. Today* 53 (1999) 575.
- [35] A. Cabañas, J.A. Darr, E. Lester, M. Poliakoff, J. Mater. Chem. 11 (2001) 561.
- [36] M. Fernández-García, A. Martínez-Arias, A. Iglesias-Juez, A.B. Hungria, J.A. Anderson, J.C. Conesa, J. Soria, *Appl. Catal. B: Environ.* 31 (2001) 39.
- [37] M. Hirano, T. Miwa, M. Inagaki, *J. Solid State Chem.* 158 (2001) 112.
- [38] A.I. Kozlov, D.H. Kim, A. Yezerets, P. Andersen, H.H. Kung, M.C. Kung, *J. Catal.* 209 (2002) 417.
- [39] M. Alifanti, B. Baps, N. Blangenois, J. Naud, P. Grang, B. Delmon, *Chem. Mater.* 15 (2003) 395.
- [40] T. Mokkelbost, I. Kaus, T. Grande, M.A. Einarsrud, *Chem. Mater.* 16 (2004) 5489.
- [41] Y. Guo, G. Lu, Z. Zhang, S. Zhang, Y. Qi, Y. Liu, *Catal. Today* 126 (2007) 296.
- [42] B. Zhao, G. Li, C. Ge, Q. Wang, R. Zhou, *Appl. Catal. B: Environ.* 96 (2010) 338.
- [43] H. Kishimoto, T. Omata, S. Otsuka-Yao-Matsuo, K. Ueda, H. Hosono, H. Kawazoe, *J. Alloys Compd.* 312 (2000) 94.
- [44] Z. Zhang, X. Yan, B. Tian, C. Yu, B. Tu, G. Zhu, S. Qiu, D. Zhao, *Micropor. Mesopor. Mater.* 90 (2006) 23.
- [45] R. Feng, X. Yang, W. Ji, C. Au, *Mater. Chem. Phys.* 107 (2008) 132.
- [46] M. Goto, Y. Machino, T. Hirose, *Micropor. Mater.* 7 (1996) 41.
- [47] M.R. Álvarez, A.R. Landa, L.C. Otero-Díaz, M.J. Torralvo, *J. Eur. Ceram. Soc.* 18 (1998) 1201.
- [48] F. Zhang, Y. Yan, H. Yang, Y. Meng, C. Yu, B. Tu, D. Zhao, *J. Phys. Chem. B* 109 (2005) 8723.
- [49] K.S.W. Sing, D.H. Everett, R.A.W. Haul, L. Moscou, R.A. Pierotti, J. Rouquerol, T. Siemienińska, *Pure Appl. Chem.* 57 (1985) 603.
- [50] D. Zhao, Q. Huo, J. Feng, B.F. Chmelka, G.D. Stucky, *J. Am. Chem. Soc.* 120 (1998) 6024.
- [51] D. Zhao, J. Sun, Q. Li, G.D. Stucky, *Chem. Mater.* 12 (2000) 275.
- [52] G. Leofanti, M. Padovan, G. Tozzola, B. Venturelli, *Catal. Today* 41 (1998) 207.
- [53] M. López Granados, A. Gurbani, R. Mariscal, J.L.G. Fierro, *J. Catal.* 256 (2008) 172.
- [54] J. Kim, W. Myeong, S. Ihm, *Appl. Catal. B: Environ.* 71 (2007) 57.
- [55] H. Wang, Z. Zhao, C. Xu, J. Liu, J. Liu, *Catal. Lett.* 102 (2005) 251.
- [56] J. Liu, Z. Zhao, C. Xu, H. Wang, *React. Kinet. Catal. Lett.* 87 (2005) 107.
- [57] L. Xiao, K. Sun, X. Xu, X. Li, *Catal. Commun.* 6 (2005) 796.
- [58] H. Wang, Y. Chen, Q. Zhang, Q. Zhu, M. Gong, M. Zhao, *J. Nat. Gas. Chem.* 18 (2009) 211.
- [59] P.S. Lambrou, A.M. Efstathiou, *J. Catal.* 240 (2006) 182.
- [60] C. Bozo, N. Guilhaume, J.M. Herrmann, *J. Catal.* 203 (2001) 393.
- [61] P. Fornasiero, J. Kašpar, V. Sergio, M. Gaziani, *J. Catal.* 182 (1999) 56.
- [62] P. Fornasiero, N. Hickey, J. Kašpar, C. Dossi, D. Gava, M. Graziani, *J. Catal.* 189 (2000) 326.
- [63] J. Fan, X. Wu, Q. Liang, R. Ran, D. Weng, *Appl. Catal. B: Environ.* 81 (2008) 38.
- [64] F. Fally, V. Perrichon, H. Vidal, J. Kašpar, G. Blanco, J.M. Pintado, S. Bernal, G. Colon, M. Daturi, J.C. Lavalley, *Catal. Today* 59 (2000) 373.
- [65] I. Atribak, A. Bueno-López, A. García-García, *J. Catal.* 259 (2008) 123.
- [66] J. Wang, M. Shen, Y. An, J. Wang, *Catal. Commun.* 10 (2008) 103.
- [67] M. Zhao, M. Shen, J. Wang, *J. Catal.* 248 (2007) 258.
- [68] R.A. Daley, S.Y. Christou, A.M. Efstathiou, J.A. Anderson, *Appl. Catal. B: Environ.* 60 (2005) 117.
- [69] N. Hickey, P. Fornasiero, J. Kašpar, J.M. Gatica, S. Bernal, *J. Catal.* 200 (2001) 181.
- [70] S.Y. Christou, C.N. Costa, A.M. Efstathiou, *Top. Catal.* 30/31 (2004) 325.
- [71] C.N. Costa, S.Y. Christou, G. Georgiou, A.M. Efstathiou, *J. Catal.* 219 (2003) 259.
- [72] G. Chen, W.T. Chou, C.T. Yeh, *Appl. Catal.* 8 (1983) 389.
- [73] C. Descorme, R. Taha, N. Mouaddib-Moral, D. Duprez, *Appl. Catal. A: Gen.* 223 (2002) 287.
- [74] M. Boaro, F. Giordano, S. Recchia, V.D. Santo, M. Giona, A. Trovarelli, *Appl. Catal. B: Environ.* 52 (2004) 225.
- [75] S. Hilaire, X. Wang, T. Luo, R.J. Gorte, J. Wagner, *Appl. Catal. A: Gen.* 215 (2001) 271.